Direct observation of the elasticity-texture relationship in pyrolytic carbon via in situ micropillar compression and digital image correlation

Joey Kabel [a, *], Thomas E.J. Edwards [b, **], Amit Sharma [b], Johann Michler [b], Peter Hosemann [a]

[a] University of California Berkeley, Department of Nuclear Engineering, 4151 Etcheverry Hall, Berkeley, CA, 94720, USA
[b] Laboratory for Mechanics of Materials and Nanostructures, Empa Swiss Federal Laboratories for Materials Science and Technology, CH-3602 Thun, Switzerland

ARTICLE INFO

ABSTRACT

Pyrolytic carbon (PyC) plays a critical role in many applications for its unique properties. In ceramic composite systems, the elastic properties of PyC at the fiber/matrix interface drive toughening mechanisms, enabling structural performance at increased operating temperatures. PyC expresses a wide range of crystallographic texture depending on fabrication parameters. As a result, modelling and optimization requires direct understanding of the texture-property relationships at the relevant length scales. This research leverages high-resolution transmission electron microscopy (HRTEM) to link the PyC microstructure to the elastic response observed via digital image correlation (DIC) during micropillar compression. The HRTEM and DIC results quantitatively resolve a gradient for microstructural texture and Young's modulus respectively, showing that disordered texture increases compressive stiffness normal to the average orientation of the PyC basal planes. The values for modulus ranged from 55 to 150 GPa, which are large compared to most experimental methods, but may be more realistic considering the uniaxial stress state and length scale. The behavior supports findings from numerical homogenization models, suggesting that this advanced technique may provide a path forward for optimization and validation of these nanoscale elasticity models.

© 2021 The Author(s). Published by Elsevier Ltd. This is an open access article under the CC BY license (http://creativecommons.org/licenses/by/4.0/).

1. Introduction

Pyrolytic carbon (PyC) is used in myriad applications from medical devices to nuclear fuel [1,2]. In high performance composites, PyC is commonly integrated via chemical vapor infiltration (CVI) as a thin (5–2000 nm) bond layer between the fiber and matrix to promote crack deflection and composite toughness [3]. This bond layer creates a series of interfaces referred to as the interphase. Knowledge of the elastic properties of the interphase is critical in any effort to predict composite behavior. This is true whether considering models for interfacial crack deflection or evaluating component-scale stress and strain distribution [4–6].

CVI PyC can be described as a stochastic arrangement of graphite planes, organized in nanometer scale domains that are, on average, stacked parallel to the deposition surface, the fiber in this case. Typically, the surface roughness of the fiber results in a texture gradient that may influence the local properties [7,8]. The relative disorder of these domains is most commonly characterized in terms of the orientation angle (OA), obtained using high resolution transmission electron microscopy (HRTEM) with Fast Fourier Transform (FFT) analysis or selected area electron diffraction (SAED) [9–11]. Texture classification proposed by Reznik and Hüttinger [12,28] includes high texture (HT, OA < 50°), medium texture (MT, 50° < OA < 80°) and low texture (LT, 80° < OA < 180°). Many methods have been explored to evaluate the Young's modulus of PyC including macroscopic tensile, compression, and

---

* Corresponding author.
** Corresponding author.
E-mail addresses: joey.kabel@berkeley.edu (J. Kabel), Thomas.Edwards@empa.ch (T.E.J. Edwards).

resonant spectroscopy methods [13–15], as well as nano-indentation and microcantilever bending [16,17]. However, finding a direct link between the texture and resulting elastic properties has proved challenging [18]. Additional microstructural and chemical parameters such as the domain width (L_a) and domain height (L_c), interplanar spacing d_{002}, and hydrocarbon content as they relate to cross-linking and interstitial defects can influence the contribution of different stiffness tensors. Farbos, Stein, and Savini et al., have explored these relationships, suggesting dependencies of out of plane stiffness on L_c, where reduced L_c increase the number of cross-linking there by stiffening the matrix [14,19,20]. Typical methods for identifying L_a and L_c include X-ray diffraction, Raman spectroscopy, and image processing techniques using HRTEM [10,19,21,22]. X-ray photo-electron spectroscopy is another excellent tool to describe local structure with additional information on chemical composition. However, these techniques have relatively large spot size compared to HRTEM, limiting spatial resolution of the microstructure across small multiphase coatings.

It can be useful to discuss the elastic constants of PyCs with those of graphite, where OA approaches zero. As a transversely isotropic material, graphite expresses a high degree of anisotropy where theoretical Young's Modulus varies from E_x ~1000 GPa parallel to the basal planes to E_z ~25 GPa normal to the basal planes. However, most experimental results for PyC find values for both in plane (E_x) and out of plane (E_z ranging from ~5 to 50 GPa, regardless of experiment type and graphitic domain orientation [14,17,19,20,23]. A few studies have been able to extract properties that align closer to the predicted in-plane values reaching ~100–300 GPa [15,24]. The variability between experiment type, and often muted dependency on graphitic orientation, becomes particularly concerning when evaluating microscale applications of PyC such as the composite interphase where PyC thickness is often <1 μm [3,25].

Typically, nanoindentation has been used to evaluate PyC at this length scale. Nanoindentation can provide unique spatial resolution of elastic constants, however, pyrolytic carbon exhibits nearly reversible elastic response making it challenging to accurately apply the analysis methods that were originally developed for plastic materials [18]. Several researchers, summarized by Gross et al., have explored new models to capture the true contact area and elastic response [16]. It was concluded that measurements in the E_z direction were considered valid as it was possible to match expected properties, while measurements in the $E_{x,y}$ directions were misleading due to nano-buckling mechanisms. It was shown that sharp indenters can also cause complex stress states that promote plane rotation with accompanied basal plane slip and nano-buckling [18,23]. These mechanisms in conjunction with in-plane defects such as cross-linking and interstitials are suggested to be responsible for the moduli, hysteresis, and anelastic recovery [18,26]. Because the anelastic behavior is observed regardless of basal plane orientation, it is suggested here, that the observed moduli are not only a measurement of the interatomic bond stretching (both covalent and van der Waals for PyC), but likely significantly underestimated because of the basal plane slip and buckling effects. Fig. 1 shows typical anelastic indentation curves normal and parallel to the plane for different indenter types, adapted from Gross et al. [16].

These experimental complexities have spurred alternative efforts to estimate elasticity building up from the nanoscale structure [14,20,27–29]. The overarching procedure has been to leverage HRTEM micrographs to reconstruct a descriptive microstructure that can be modelled at the atomic level or have an elasticity tensor projected on to it. Böhlke and Lin et al. approached the latter via OA and a local binary pattern (LBP) segmentation algorithm to define plane and domain orientation distribution functions (PODF & DODF) respectively [28,29]. Given the stochastic distribution,

elasticity tensors from macroscopic ultrasound phase spectroscopy of graphite and PyC could be projected on to the microstructure and homogenized. It can be noted that these projections were developed with 2D HRTEM images and assumed perfectly bonded domains with no stiffness. Farbos et al., developed 3D atomistic reconstructions of HRTEM for integration into molecular dynamic (MD) simulations [30]. Unit cells of ~6–12 nm edge length were generated for pure graphite as well as two texture domains, rough and regenerative lamellar (RL & ReL), both considered HT in the OA classification scheme. The RL and ReL cells consisted of nanosized graphene domains with boundaries consisting of lower order ring structures as well as sp^3 interplanar cross-links. These are proposed as the typical domain defects observed by HRTEM. The efforts by Lin and Farbos et al. effectively evaluated the elastic behavior of a single domain. They found strikingly similar values for all the elastic constants except C_{33} where the MD simulation showed ~30 GPa and the DODF estimated ~90 GPa. Reasoning for this discrepancy was not well understood, but both length scale and boundary condition assumptions may be playing a role. On the contrary, the Böhlke model evaluates the PODF across all domains in the 2D 50 × 50 nm^2 HRTEM images of different textures (LT, MT, and HT). The analysis provides a homogenized elasticity based on the relative contributions of the experimental elastic constants (determined macroscopically with ultrasound phase spectroscopy [13,31]) as a function of the loading direction, β. Fig. 2 summarizes the model with an estimate for the mean modulus (HS-Mean) plotted versus β, where 0° and 180° represent loading normal to the average basal plane orientation and 90° is in-plane for MT PyC.

It was found that the degree of anisotropy as a function of β is reduced by more than 80% compared to the theoretical relationship of E_x and E_z of graphite. This may explain the muted dependency on textural orientation observed across the experimental test methods. It should also be noted the modulus values here are several factors larger than many experiments. Generally, this discrepancy is attributed to large scale softening phenomena such as porosity for bulk scale tensile, compression, and resonant spectroscopy [17,28,32], and nano-buckling or basal plane slip mechanisms in the case of nanoindentation [23]. The advancement of these models may provide a new path for mapping the true effects of texture and defects on elasticity, thereby improving composite design and constituent-based modelling. The goal of this effort is to provide an experimental pathway to help refute or validate the small-scale elasticity models.

The study presented here combines micropillar compression [33] and in situ scanning electron microscopy (SEM) digital image correlation (DIC) for novel evaluation of uniaxial elastic properties across the SiC/PyC/SiC interphase. This imaging-based strain mapping method measures the total strain at the surface of a deforming sample, during both elastic and plastic loading phases [34]. It has recently been applied to micromechanical testing [35,36] with nano-scale spatial resolution [37] under a range of temperature [34,36,38] and fatigue loading [39] conditions across a variety of metals [35,40], intermetallics [36,38] and ceramics [41], and has supported modelling efforts [40,42]. The micropillar geometry and test conditions provide an idealized uniaxial stress and direct line-of-sight monitoring of the textured PyC at the micro-scale during testing. The test geometry is fabricated by focused ion beam (FIB) milling. The OA texture and domain size from HRTEM FFT provides insight to the relative defect density and orientation distribution of local domains. Ultimately, this study provides direct values for Young's modulus, and qualitative insight to the Poisson's ratio, E_z and v_{zx}, with compression orthogonal to the average basal plane orientation as a function of PyC microstructure.
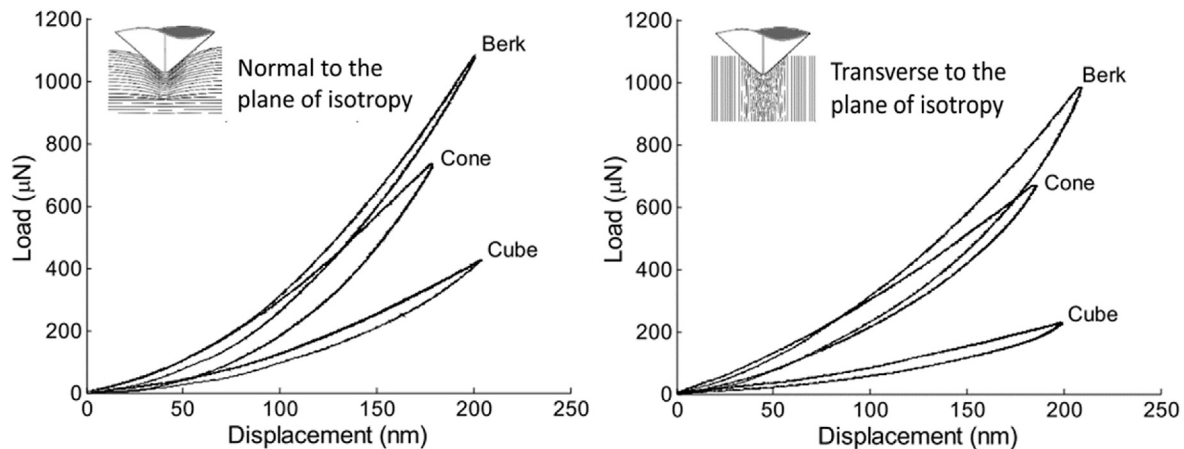
Fig. 1. Nanoindentation curves for PyC orthogonal and parallel to the average basal plane orientation. Indenter tips express reducing stiffness with increasing sharpness. Anelastic behavior is also observed showing hysteresis attributed to energy loss from frictional sliding between graphite planes. The general trend suggests that basal plane orientation is not playing a dramatic role. Reproduced and adapted with permission from Ref. [16], copyright John Wiley and Sons 2012.
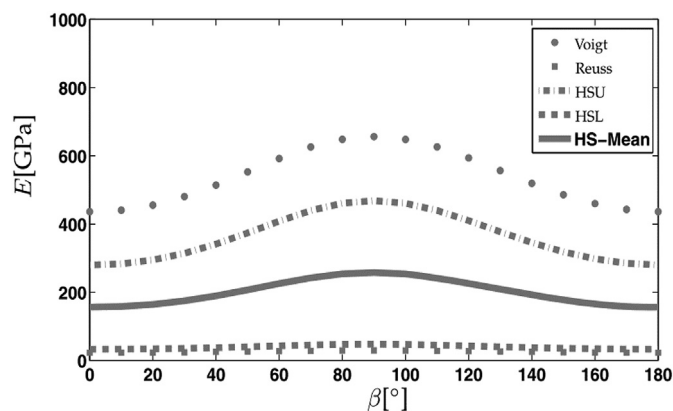
PyC	$E^{HSM}(\beta = 0°)$ [GPa]	$E^{HSM}(\beta = 90°)$ [GPa]
HT	98.55	306.01
MT	156.24	257.7
LT	170.13	248.74

Fig. 2. Homogenized elastic modulus for MT PyC based on macroscale elastic constants projected onto nanoscale PyC domains via a stochastic domain orientation distribution function. β describes the loading direction relative to the average basal plane orientation, where 0° and 180° represent loading orthogonal to the basal planes. Anisotropy is dulled and modulus values are larger than most experiments. Reproduced and adapted with permission from Ref. [28], copyright John Wiley and Sons 2012.

2. Experimental

A single fiber composite with monolayer PyC interphase, referred to as a microcomposite, was evaluated in this research. This simplified sample provided easy access to the control interphase, however, this method is also applicable to more complex composite configurations. General Atomics (GA) manufactured the composite with a Tyranno S SiC fiber [43]. CVI was used to consolidate the fiber preform by depositing a 1.2 μm monolayer of PyC followed by a dense β-SiC matrix. The Tyranno S fiber is expected to have isotropic E ~200 GPa [43,44] and CVI β-SiC E ~ 460 GPa [45]. The fibers of these composites are typically manufactured with a polymeric sizing for material handling. These fibers come from the Tyranno company that use a polyoxyethylene (POE) sizing. Prior to PyC deposition, the sizing is burned off,

leaving a 0–10 nm layer of turbostatic carbon at the fiber surface. This structure can influence the size and uniformity of the deposited PyC. However, it is still observed that the orientation of the early PyC domain growth will depend on local surface roughness and increase uniformity as deposition thickness increases [8]. A transverse cross-section and subsequent polished surface of the microcomposite is shown in Fig. 3-A. This same composite sample was also used to characterize friction behavior of the PyC interphase [46].

The sample was mounted with the longitudinal axis of the fiber parallel to the polishing plane on an aluminum SEM stub with thermoplastic mounting adhesive. Polishing was carried out via 3 μm diamond lapping film using water lubricant in a Leica EM TXP micro-polishing instrument. The integrated stereo microscope allowed the polishing to continue until the fiber was exposed, shown in Fig. 3-B. On the polished surface, two ~2.5 × 2.5 μm^2 square cross-section micropillars with height to width ratio ~2:1 were fabricated using a 30 keV gallium FIB-SEM workstation (LYRA, Tescan, Brno, Czech Republic). The pillar cross-section dimensions kept peak-to-valley fiber curvature less than 100 nm and is considered negligible for elastic modulus evaluation. The structures were milled to contain the PyC interphase at the center height of the pillar. Fillets with 1 μm radii were also milled at the pillar base to promote uniform stress gradients and reduce sink-in effects. Course and fine milling were carried out at 10 nA and 0.25 nA, respectively. Pillars 1 and 2 are shown in Fig. 4-B. SEM and TEM were carried out to evaluate the PyC thickness as microstructure.

2.1. Compression testing

In situ compression was applied in the Z-direction with a 5 μm diamond flat punch in an Alemnis standard assembly nanoindenter (Alemnis AG, Thun, Switzerland). Testing was performed in displacement control at 5 nm s^{-1}. Each pillar was incrementally loaded and fully unloaded following 50 nm steps from 100 nm to 300 nm total indenter displacement. Pillar 1 saw two additional steps to 400 nm and 500 nm. Each unloading step took the indenter tip completely out of contact with the pillar while each load step was held at constant displacement via an integral gain feedback loop. At each step, two 512 × 512 px^2, 320 μs px^{-1} dwell, high-resolution SEM images were taken; one with the SEM raster direction parallel to the Z axis, and another with 90° scan rotation and raster direction parallel to the X axis. This was done because it has
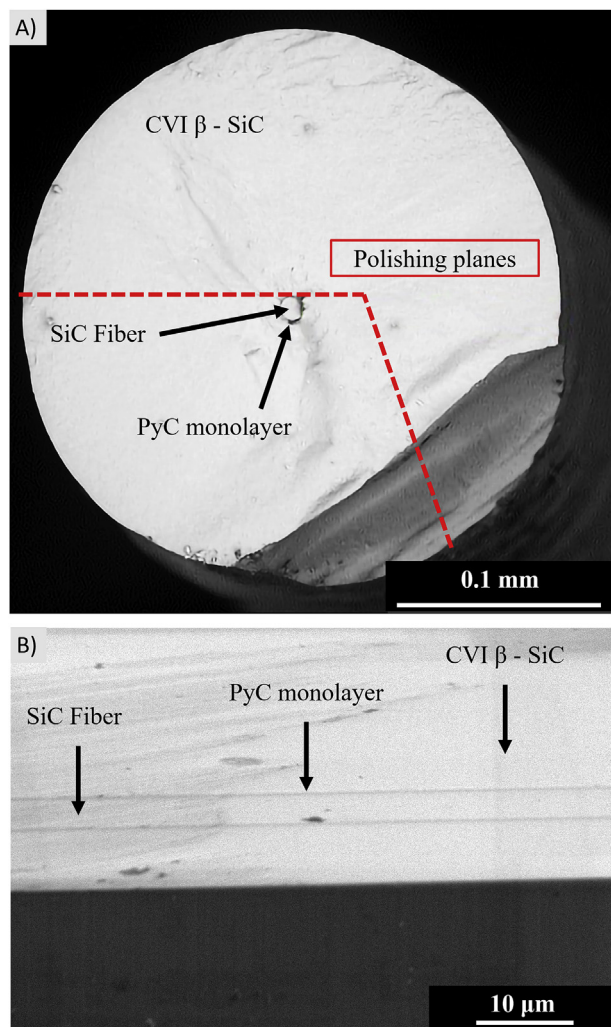
Fig. 3. A) Transverse cross-section of SiC/PyC/SiC microcomposite, red dotted lines represent polishing planes. Courtesy of GA. B) Longitudinal polished cross section showing single Tyranno S fiber embedded in a monolayer CVI PyC and β-SiC matrix. (A colour version of this figure can be viewed online.)

been found that strain mapping is more accurate when evaluated in the raster direction. SEM images were taken at 40k × magnification achieving 7.05 nm px^{-1} resolution. The axial displacement, δ_z, of the pillar was processed with Alemnis software to subtract out known machine compliance as well as account for pillar sink-in following the Zhang-Sneddon model for pillars with fillet radii assuming a continuous 3D substrate [47,48]. It should be noted here that the pillars were fabricated in a way that the substrate material in the front and behind the pillar was removed, leaving it effectively on a wall. This may result in a slight overestimation of strain in the pillar and thereby underestimation of the elastic modulus. Load drift of ~3 μN s^{-1} was found during the ~300 s compression hold for SEM imaging and was subtracted out. Fig. 4-A shows all 8 loading steps with compliance-adjusted displacement for pillar 1. Step naming is outlined in Fig. 4-D.

2.2. DIC analysis

DIC strain mapping of the pillar surface required a high-density distribution of platinum (Pt) dots. These were e-beam deposited with ~40 nm diameter using an SEM gas injection system. The beam parameters, bitmap pattern, and analysis methodology followed that
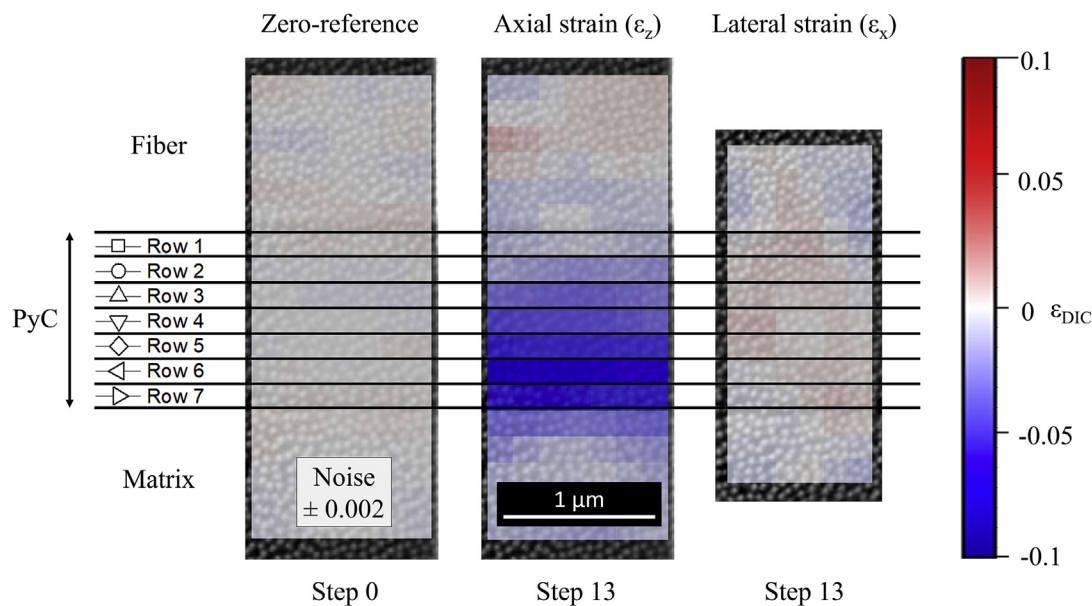
of previous research [35,36]. Pt dots are assumed non-deformable. The strain analysis was carried out using commercial software (DaVis, LaVision). Image filtering was required to normalize the brightness/contrast and bring out the speckle pattern with uniform grayscale, shown in Fig. 4-C. The images were ordered in the software following the test sequence and then shift and rotation corrected to map the speckles from image to image. Mapping was done using 24 × 24 px^2 subsets with 0% overlap to give a spatial resolution of 0.169 × 0.169 μm^2. Dots at the pillar edge were challenging to resolve and subsets were omitted from the strain analysis. 2-D strain was then calculated for each subset at each step relative to the first unloaded image. Ultimately, the PyC thickness was described by seven 1 × 7 subset rows, each equating to ~0.17 μm height and 1.18 μm wide. Each row was then averaged to explore lateral, ε_x and axial strain, ε_z, as a function of distance from the fiber surface. Row 1 has its outmost image pixels aligned with the fiber/PyC interface such that it is the first subset row within the PyC layer, and row 7 is the last within the PyC layer and borders the matrix/PyC interface. To quantify the precision of the software tool, two identical unstrained images were taken prior to testing to establish a zero-strain reference. The standard deviation was calculated by evaluating all 2-D strain subsets of the second image relative to first, representing noise due to image quality and processing. The standard deviation in the normal strain component parallel to the imaging raster direction was found to be ±0.002, and subsequently propagated through subset averaging. Raw values for compressive strain are shown in blue in Fig. 5 as negative but were analyzed later as positive for typical stress vs strain calculations. The Pt speckle pattern, zero-strain reference map, and lateral and axial strain map for the last step of pillar 1 are shown in Fig. 5 with overlaid rows.

2.3. Characterization

TEM lamella of pillar 1 after compression, and a pristine location adjacent to the pillars were fabricated to quantify the PyC texture and domain size as a function of distance from the fiber surface. The HRTEM images were acquired using a Themis 200 G3 spherical aberration-corrected (probe) TEM operating at 200 kV. Three columns by ten rows of micrographs were acquired across the PyC thickness for both samples. Each column was spaced approximately ~1 μm apart. Within each column, the average spacing between rows was approximately 100 nm, with an HRTEM field of view of 40x40 nm^2. Image spacing was controlled using set travel distance with the sample holder motor. The first image on the fiber side was taken approximately 20 nm away from the actual surface as to avoid influence from residual turbostratic carbons due to decomposition of the POE during manufacturing [8]. See Fig. 6A for a schematic layout of image acquisition. The beam condition (convergence = 6.3 mrad) and image acquisition speed (1 s to limit beam damage) were kept constant for all the scans to improve the analysis accuracy. The texture analysis of the pristine sample was also performed using selected area electron diffraction (SAED) patterns collected across 3 columns and 5 rows in the pristine sample using an aperture of 150 nm. Here, the HRTEM FFT OA method [9,31,49,50], may include contributions to the OA from small variations in foil thickness and focal depth between regions imaged across the PyC layer. The larger sampling region and parallel beam of SAED helps provide confidence in the localized sampling of HRTEM FFT. Each HRTEM FFT and SAED ring pattern was analyzed in OriginPro using the Azimuthal Average Tool to extract the average grayscale intensity of the (002) diffraction arc as a function of angle within the defined concentric circles. The peaks were fit with a Gaussian and the OA was taken as the average FWHM of the two peaks. The three images in each row for SAED and HRTEM FFT were respectively averaged, providing
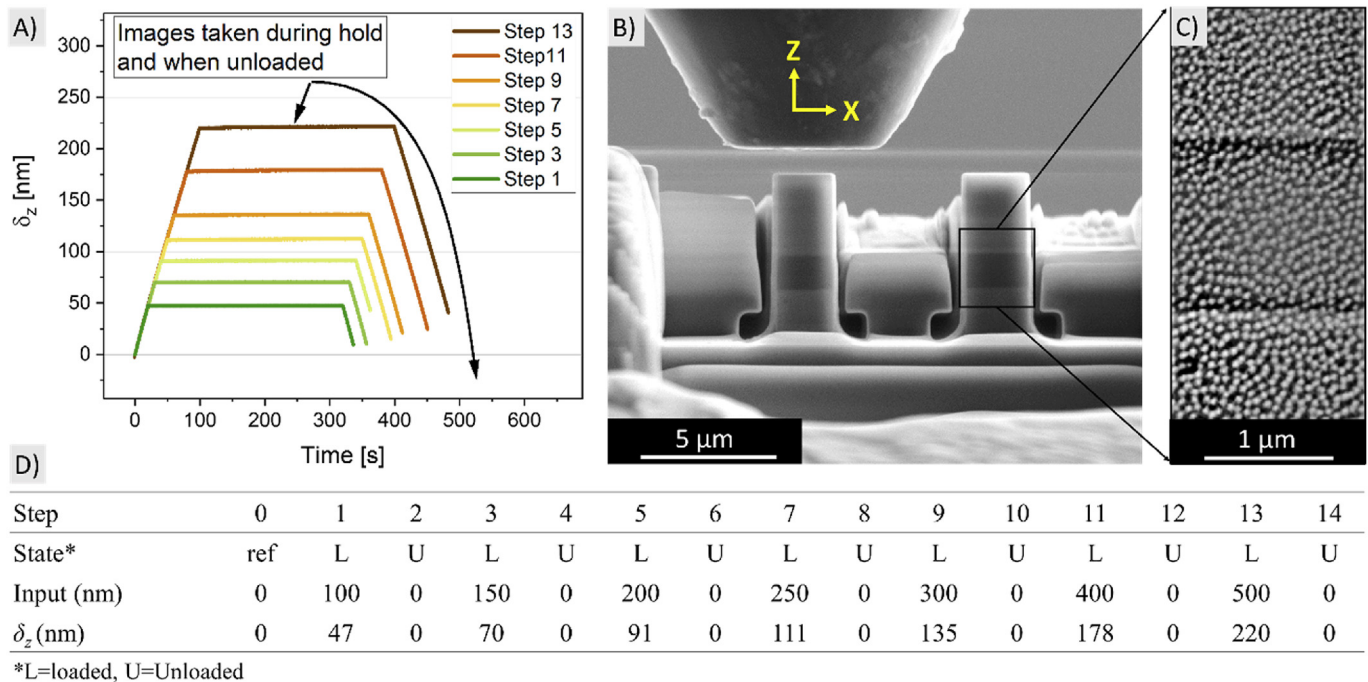
Fig. 4. A) Test sequence of pillar 1, showing displacement steps, hold for SEM image capture, and unloading. B) SEM image of both pillar 1 and 2 prior to testing. The Z and X directions are overlaid for reference throughout the paper. C) High resolution SEM image of the Pt speckle pattern applied to the pillar surfaces for DIC strain mapping. D) Loading and unloading steps. (A colour version of this figure can be viewed online.)

D)

Step	0	1	2	3	4	5	6	7	8	9	10	11	12	13	14
State*	ref	L	U	L	U	L	U	L	U	L	U	L	U	L	U
Input (nm)	0	100	0	150	0	200	0	250	0	300	0	400	0	500	0
δ_z (nm)	0	47	0	70	0	91	0	111	0	135	0	178	0	220	0

*L=loaded, U=Unloaded

Fig. 5. SEM images of DIC speckle pattern on pillar 1 with overlaid strain maps. The reference and final step are shown. Rows are dived by horizontal black lines that span the height of the PyC section of the pillar. The color of each subset is based on strain at its center point. (A colour version of this figure can be viewed online.)

representative texture as a function of distance from the fiber surface. All diffraction arcs showed consistent positioning, suggesting the basal planes were on average aligned parallel with the fiber surface.

For rows 2, 5, and 9 of the HRTEM images, a minimum of 125 clearly identifiable domains were manually traced across the three images, Fig. 6C. The domains were extracted using FIJI image processing software and fit with an ellipse to estimate L_c (long axis) and L_a (short axis), providing insight to domain size evolution across the PyC thickness [51]. Fig. 6 compiles a representative

HRTEM image, HRTEM FFT and OA Gaussian fit, SAED pattern with OA, and domain tracing from a region at the center of the pristine PyC bond layer.

3. Results

3.1. PyC modulus from load vs displacement output

From the machine output, the compliance-corrected engineering stress-strain curves for all steps of pillar 1 and 2 are presented in
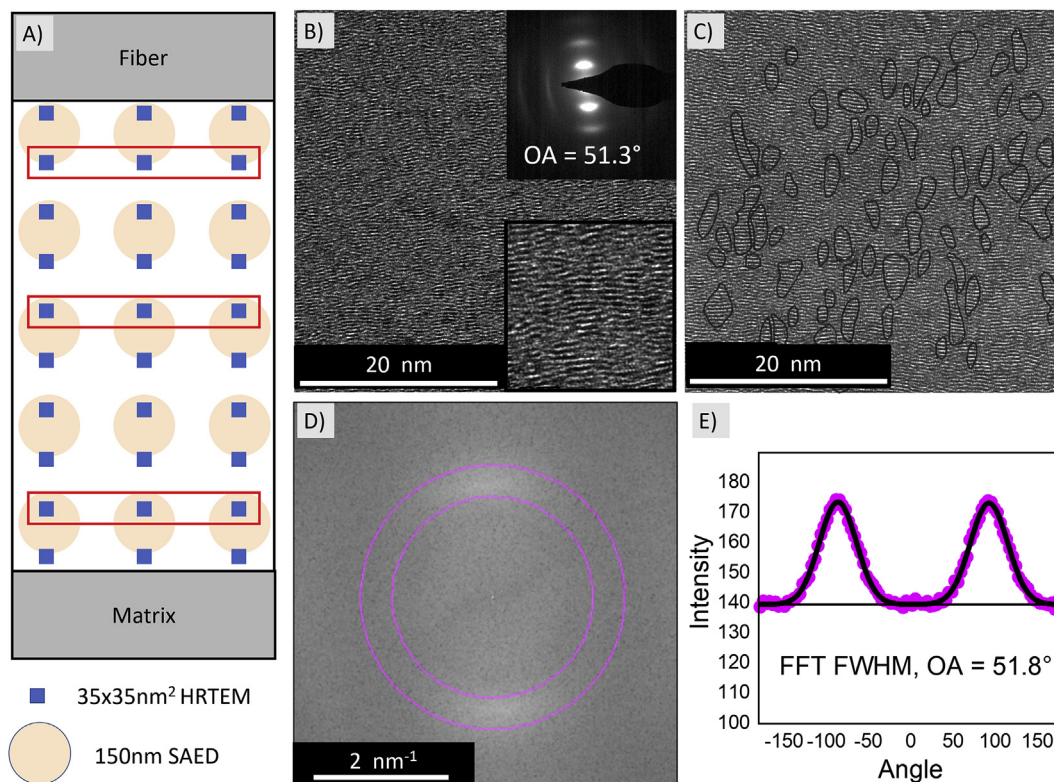
Fig. 6. A) Schematic of HRTEM and SAED acquisition locations across the PyC. The red outlines represent the image location in images in B, C, and D. B) 40×40 nm^2 HRTEM with embedded 10×10nm region showing observable (002) lattice fringes and domains. Also embedded SAED pattern with OA value of the same region. C) HRTEM with manually traced domains. D) HRTEM FFT of image B representing frequency information of the lattice fringes. E) Azimuthal Average Tool provides a Gaussian fit to the averaged grayscale intensity in the probed region (concentric pink circles) of the FFT pattern. (A colour version of this figure can be viewed online.)

Fig. 7. The behavior is repeatable and shows limited hysteresis, contrary to typical observations in nanoindentation.

For each step, the pillar modulus is evaluated on the initial ~25% of the unloading curve, shown shifted for steps 1, 5, 9, and 13 in Fig. 7. Pillar 1 and 2 are in reasonable agreement showing a dependence of total modulus on strain going from ~100 to 165 GPa. The elastic modulus orthogonal to the average basal plane orientation of the PyC, E$_{PyC}$, is extracted using an idealized spring model shown in Fig. 8, where k is the constituent stiffness, h is constituent height, and the area A cancels out. Height dimensions and constituent moduli are tabulated, and the respective moduli for the total pillar and the PyC are plotted in Fig. 8. Linear behavior is observed showing E$_{PyC}$ range from expected values ~25 GPa to upper bound values ~65 GPa. Ultimately the model assumes the evolving modulus is intrinsic to the PyC. DIC sheds light on and supports this assumption.

3.2. In situ strain mapping by DIC

The raw DIC data for axial strain of pillar 1 is plotted in Fig. 9. At each step, the average value of a given subset row is shown. The raw data was then adjusted per two observations. The first was noise subtraction by zeroing the values observed around the first unload step and subtracting this from the other unloaded steps. The second was related to the observation of permanent deformation. Although some values are below the noise level (0.002), the trend of incremental increase of the saw-tooth baseline appears strong enough to suggest a real phenomenon and warrant subtraction. This is shown in Fig. 9 for row 6 along with a strain map of the final unloading step that shows the distribution of the permanent strain. The error bars shown represent the standard deviation when
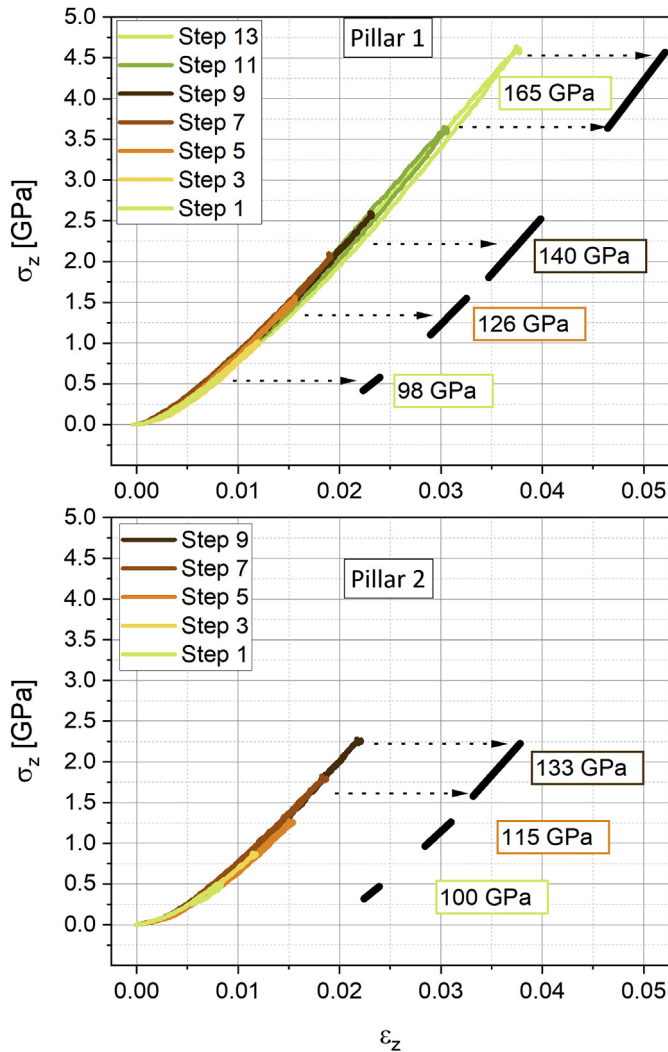
averaging the 7 subsets of each row. The mechanisms for plastic deformation may be a result of defect compression such as nanoporosity or interplanar slip of domain boundaries with significant basal rotation. The lateral DIC data did not show measurable permanent deformation, and only received initial noise adjustment.

The processed data for the observed axial and lateral strain in pillars 1 and 2 is shown in Fig. 10. The axial data shows strong sawtooth behavior with values well above the noise across loading and unloading steps, suggesting the data is real and accurate. The strain also has a spatial dependence, showing rows closer to the fiber (rows 1 and 2) having less strain than those towards the matrix, implying a stiffness gradient. This is visualized in the 2-D strain map shown in Fig. 5. Furthermore, these same data points show a slight reduction in strain over the last two loading steps which suggests that stiffness is evolving with increasing stress, similar to the observations from the machine output.

The lateral strain is an order of magnitude smaller with significantly more scatter. However, the same saw tooth behavior of the loading schedule is present, and values associated with the highest loads rise above the noise threshold. Additionally, the lateral strain shows an increasing trend with increasing load, highlighted by a red line for reference. Considering this, it is likely that the values observed are real, though should be taken cautiously when discussing the Poisson ratio. Two SEM images for the lateral strain were of noticeably poorer quality, highlighted by blue circles, and were hence not considered when evaluating the Poisson's ratio.

Data processing revealed that the boundary rows, 1 and 7, consistently deviated from trends observed in the more central rows. For example, strain at row 7 decreased from row 6, and hence deviated from the increasing trend seen moving away from the fiber. Also, the error in these rows was consistently larger. These

Fig. 7. Compliance corrected compressive stress-strain curves for pillar 1 and 2. The elastic modulus is extracted based on the initial 25% of the unloading curve and plotted for every other step to highlight the evolving modulus with increased pressure. (A colour version of this figure can be viewed online.)

equal to 0.08 μm for row one.

The DIC strain ε_z is plotted versus the stress, σ_z, in Fig. 12. Pillar 1 and 2 show similar behavior through $\sigma_z < 2.25$ GPa. Both show reducing modulus moving away from the fiber (row 2 → 6), pillar 1 shows a more pronounced trend. Above 2.25 GPa, pillar 1 shows an inflection with increasing stiffness. This inflection becomes more dramatic and potentially unrealistic for rows 2 and 3, showing a modulus of ~450 GPa for row 3. There are likely two factors contributing to this transition. The first is assumed to be a real evolution of intrinsic stiffness, observed in the machine output data as well, mechanisms for which are discussed later. The second is that as the intrinsic stiffness increases, it becomes more challenging for the DIC to resolve the resulting smaller strains with accuracy. This is supported by the fact that the software was unable to properly track (observe saw-tooth behavior with strain magnitude $\gg 0.002$) the elastic strain for the SiC fiber (E ~ 200 GPa) or matrix (E ~ 460 GPa). If we consider the regions prior to the inflection point (loaded to less than 2.25 GPa), the largest modulus supporting a linear trend is observed for row 2 with E ~ 150 GPa. This can be considered an upper bound limit for measurable elastic modulus given the experimental conditions of this study. With that considered, the moduli for each row of pillar 1 and 2 in are fit on Fig. 12 for $\sigma_z < 2.5$ GPa. Rows 5 and 6 of pillar 1 are also fit after the inflection region (light gray) since the modulus values are less than the defined upper bound. The comparable moduli are summarized and plotted with respect to row and estimated distance from the fiber surface.

3.3. Texture and domain size analysis by TEM

Fig. 13A plots the SAED and HRTEM FFT OA for the pristine PyC. The values are in good agreement with similar levels of noise, suggesting that the averaged HRTEM FFT OA at equidistance from the fiber adequately describes the global texture in that region. The HRTEM approach allows for improved spatial resolution of OA and domain size across the PyC thickness. The HRTEM FFT OA for pillar 1 shows increased magnitude and rate of change across the thickness compared to the pristine PyC. Without textural data of pillar 1 prior to deformation, it is not possible to identify if the relative disorder evolved during compression, or if it is simply due to non-uniformities during deposition. Although some plastic deformation was observed in the DIC, for the sake of discussion, it is assumed that deposition non-uniformities are responsible. In situ TEM compression testing may provide the data needed to verify or refute compression induced deformation. Fig. 13B and C plot the pristine condition graphene domain data extracted from the HRTEM locations highlighted in red. The average height, L_c, of the domains decreased marginally from fiber to matrix (2.4–2.1 nm), whilst the average domain width, L_a, remained nearly unchanged at ~1.2 nm. This is supported by previous work on this exact PyC by Kabel et al. [46], with Raman analysis that identified the D and G band intensities (I_G and I_D) on a pristine fracture surface at the midpoint of this PyC bond layer (see Figs. 5 and 17 in Ref. [46]). According to the Tuinstra-Koeing formula for nanocrystalline graphite, the ratio of the band intensities (I_D/I_G) is proportional to $1/L_a$ [52]. The previous work found $I_D/I_G = 0.76$, or equivalently $L_{\bar{a}}$ 1.3 nm, which is in great agreement with the values measured here by HRTEM tracing. One may also note a 25% decrease in the standard deviation of values measured for L_c, whilst L_a increases by a negligible 2%, indicating the shape of the grains become progressively more uniform with deposition thickness. To summarize the combined microstructural information, the fiber side of the PyC consists of less uniform, slightly elongated, and more misoriented domains compared to the matrix side. Regarding microstructural influence on elastic modulus, several authors have identified that

artifacts are likely attributed to two processes. First, the elastic mismatch (stiffer SiC) at the interface can act as a constraint for material displacement, this is discussed with more detail in section 4. The second relates to DIC processing as the edges of each subset may partially overlap into the boundary SiC at the interface. In both cases, the 2-D strain output is likely to underestimate the true strain of the PyC due to the adjacent stiff SiC. As a result, rows 1 and 7 are omitted in following analyses.
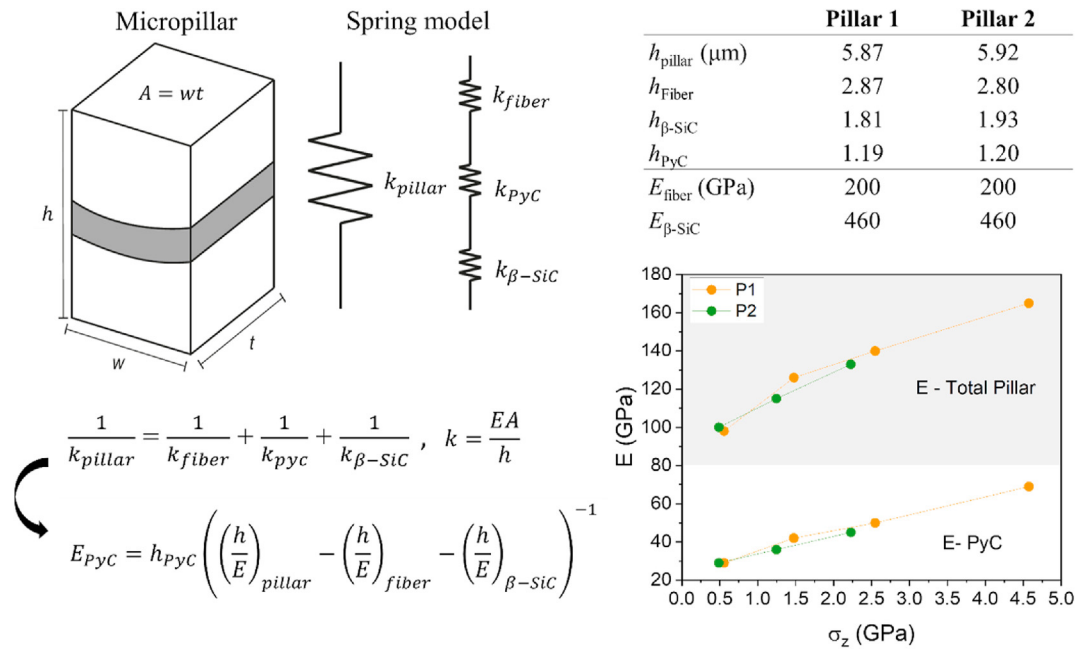
The Poisson ratio, $v_{zx} = \varepsilon_x/\varepsilon_z$ is taken for all loading steps beyond the noise-normalized point and after the low-quality SEM images, representing a region with reasonably resolved strain values. Fig. 11 presents v_{zx} for rows 2–6 as a function of loaded step with propagated error from the raw data. There is a clear trend related to location in the PyC, showing reduced v_{zx} moving away from the fiber. Because there appears to be a lack of stress dependence with each increasing steps, the average for each row across all steps was taken to provide a single value. Again, the associated error is large and should be interpreted as qualitative speculation. This is plotted for pillar 1 and 2 in Fig. 11 as a function of row and estimated distance from the fiber surface. The estimated distance for a given row is assigned to the center point of the subset, hence

Fig. 8. Idealized spring model with schematic and relationship between stiffness and modulus to calculate E_{PyC}. Dimensions and literature values of modulus for the fiber and SiC matrix are tabulated. The plot shows the trend for modulus as a function of applied pressure. The spring and pillar schematic is courtesy of Daniele Casari (Empa Swiss federal laboratories). (A colour version of this figure can be viewed online.)
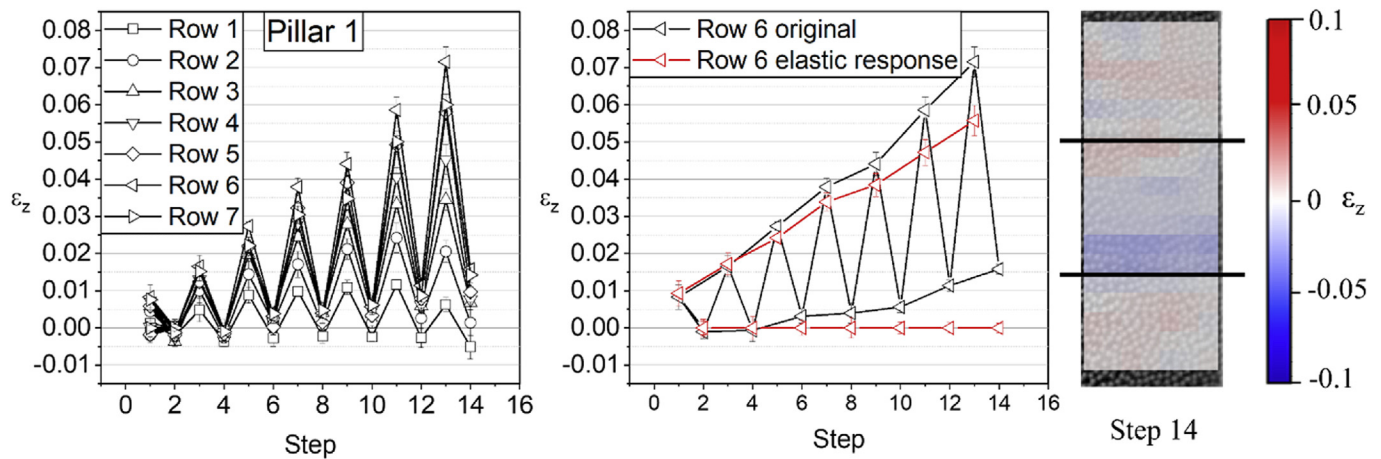

Fig. 9. A) Raw DIC data of pillar 1 showing the average strain value for each row, at each loading step. B) Row 6 of pillar 1 showing progressive permanent strain evolution following each unloading step. Plastic strain was subtracted to capture the elastic response, shown by the red plot. C) Final unloading step showing strain map with plastic deformation in the PyC near the β-SiC matrix. (A colour version of this figure can be viewed online.)

stiffness along the domain-averaged c-axis is generally independent of L_a, but inversely proportional to L_c [14,19,20,22]. This suggests that cross-linking defects at domain boundaries are a stiffening mechanism under c-axis compression. However, the stiffness range modelled by Farbos et al. for L_c = 1.5–2.6 nm is less than 5 GPa (see C33 dependence in Figs. 4 and 5) in Ref. [14]. The same study suggests that a three degree change in intergrain misorientation (equivalent to ΔOA ~5° [21]) can change stiffness by 20–50 GPa depending on the axis of loading. As a result, it is expected that the L_c values observed here have a negligible influence on stiffness, and that OA is dominating observed change in E_z. As such, the discussion focuses on the OA structure-property relationships.

4. Discussion

The machine output showed continuous evolution of E_{PyC} from 25 to 65 GPa for both pillars. These values are within experimental expectation but toward the upper bound. This is reasonable considering the uniaxial stress state and ~7.5 μm^3 sampling volume [17]. However, the machine output is still an indirect method to estimate the average PyC modulus, requiring compliance correction from multiple sources while also applying an idealized spring model that doesn't account for constraint and property values taken from literature. Because the pillars are fabricated on a wall, it is likely the total compliance was underestimated when following the Zhang-Sneddon model. An FEM model to capture these effects
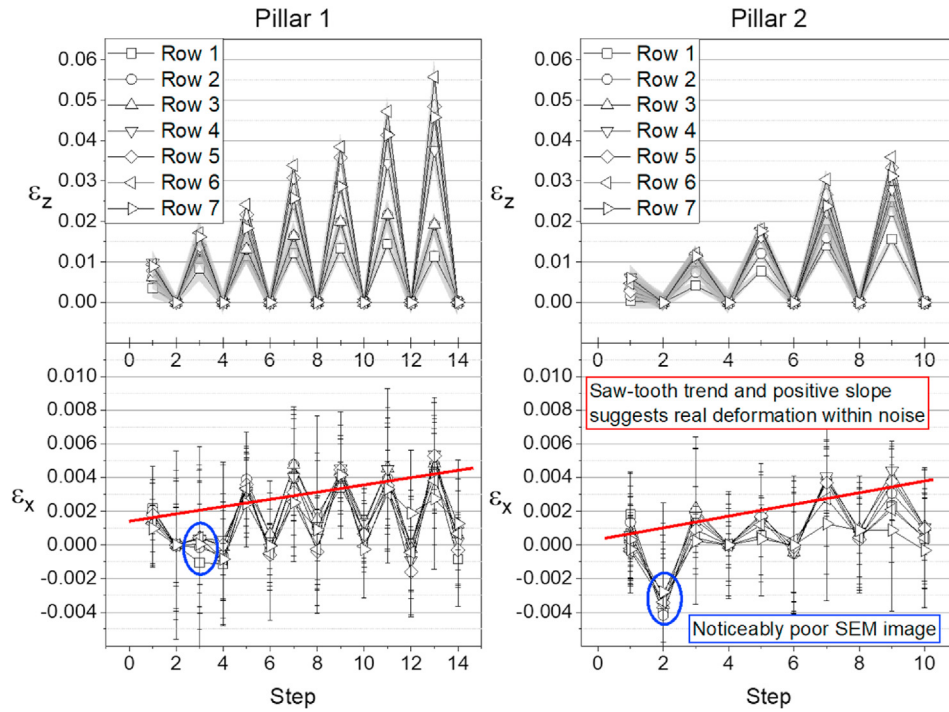
Fig. 10. Plasticity-corrected DIC axial (ε_z) and lateral (ε_x) elastic strain for pillar 1 (left) and pillar 2 (right). Red trend line follows the general evolution of lateral strain upon compressive loading. Blue circles highlight bad SEM images and resulting poor DIC output. (A colour version of this figure can be viewed online.)
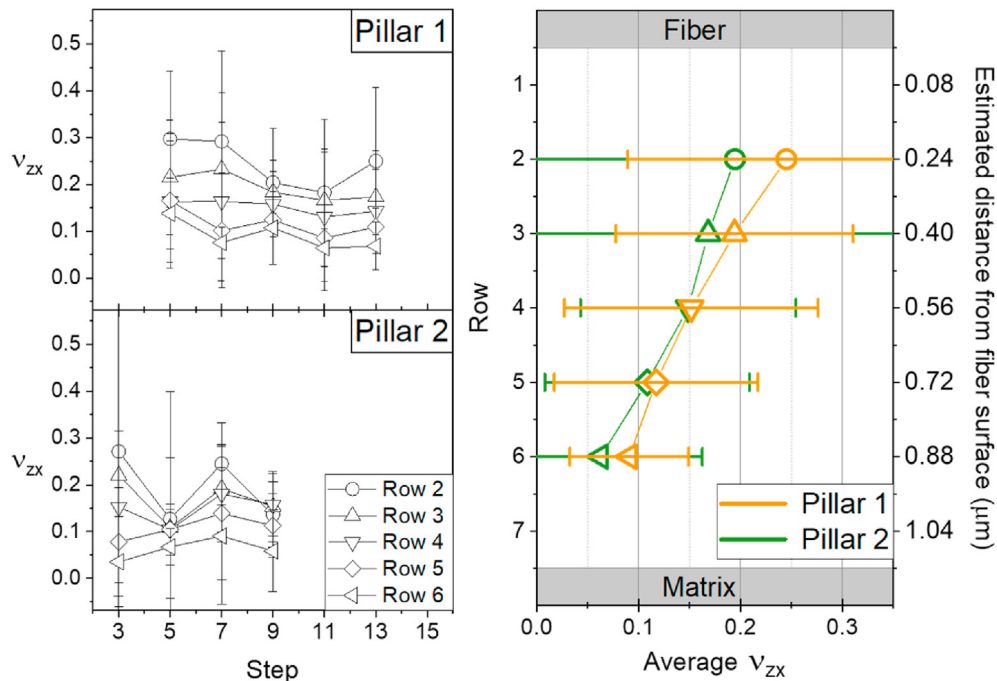

Fig. 11. (Left) Poisson ratio per row, per step, of pillar 1 and 2. (Right) Summary plot of each row averaged across all steps, plotted in relationship to the fiber and matrix boundary regions expressed in gray. (A colour version of this figure can be viewed online.)

would find increased compliance of the substrate, decreasing the corrected strain in the pillar and thereby increasing the PyC modulus. Although increasing beyond expected literature-based values, this moves closer to those found with DIC. Indeed, it is not common to measure Young's Modulus by micro-compression; one usually encounters combinations of poorly corrected substrate compliance, surface roughness and sample-indenter misalignment which complicates analysis [53]. A recent study attempted to directly measure the displacement of the interface between nanolaminates and their Si substrate pedestal during in situ SEM loading, they had some success for compliance correction, although J-shaped initial loading remained [54]. Nanoindentation
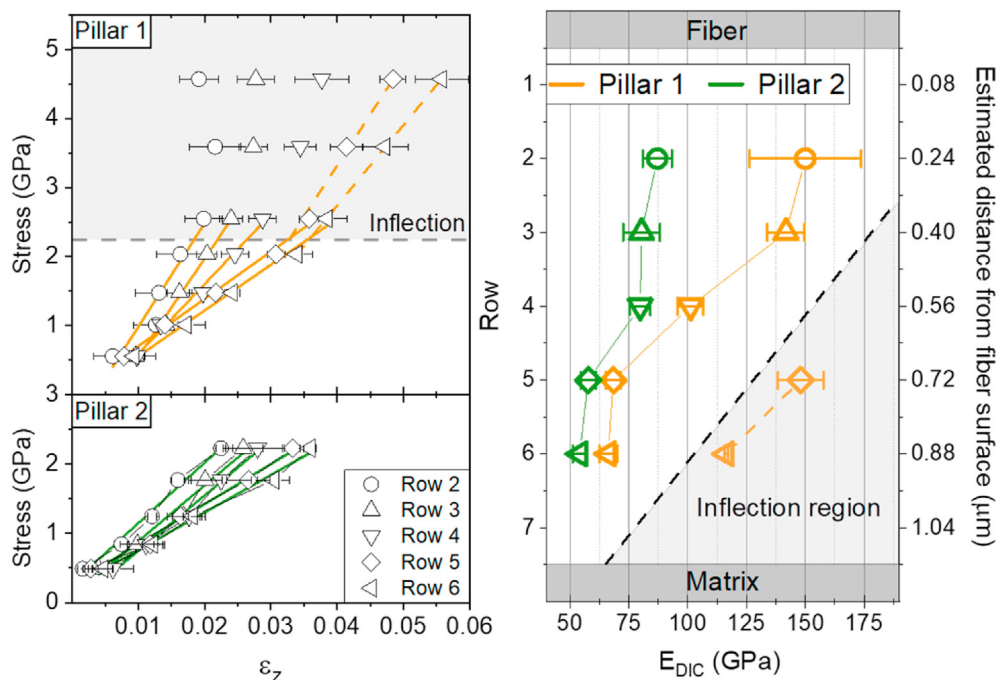
Fig. 12. (Left) DIC stress versus strain plots for all rows at each step for pillars 1 and 2. (Right) Summary plot of the DIC modulus for each row, showing a clear gradient in stiffness across the PyC bond layer. The values in the inflection region suggest an intrinsic shift in stiffness for the same row with increased pressure (>2.25 GPa). (A colour version of this figure can be viewed online.)
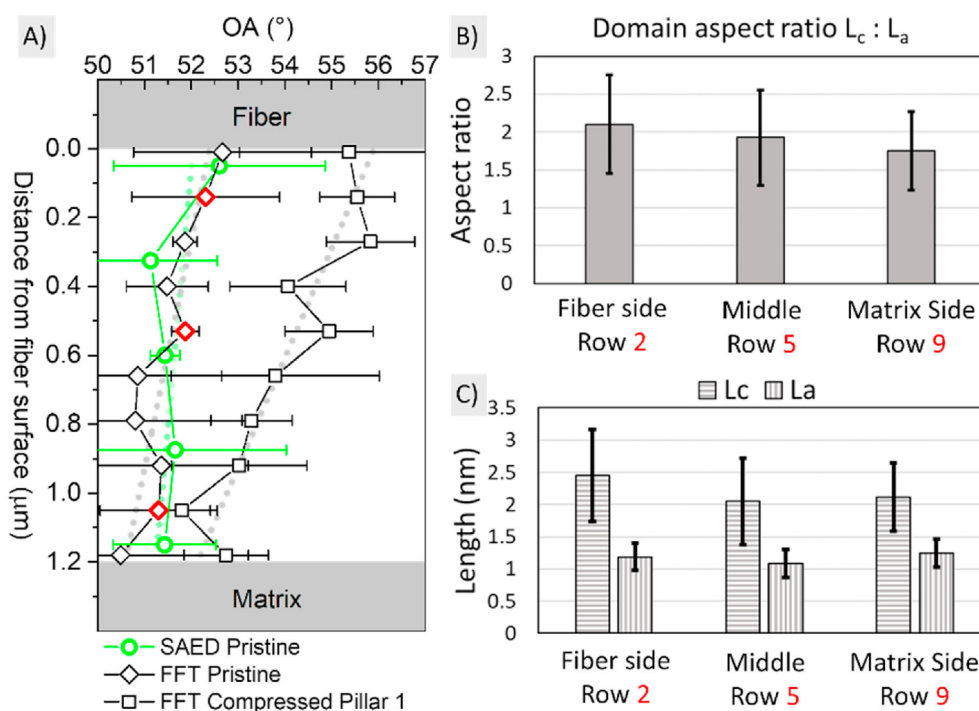
Fig. 13. A) Summary plot of OA from SAED and FFT of the pristine PyC and from FFT of pillar 1 PyC. The dotted lines are linear fits to each OA data set. B) Average aspect ratio of pristine PyC domains from the locations highlight in red. C) Average L_c and L_a of pristine PyC domains from the locations highlighted in red. The error bars represent the measured standard deviation of each quantity. (A colour version of this figure can be viewed online.)

is usually more successful for modulus measurements as compliance and tip shape are corrected for by calibration against known standards [55]. This is difficult to achieve for micro-compression given the irregularity of test geometries from FIB milling. However, the 'indentation' modulus is measured according to the multiaxial loading experienced; yet in some cases, as here, it is desirable to measure a modulus uniaxially.

The DIC method applied here is a novel approach to modulus measurement at this length scale and is shown to be an effective solution. Indeed, the 2×10^{-3} strain noise level with 170 nm spatial

resolution, achievable by DIC in the SEM raster direction, is ample to extract precise variations in the compression modulus across the 1.2 μm thick PyC layer. Imaging perpendicular to the pillar surface, in situ during each load hold, after waiting for the setup to settle for at least 12 h, avoids many of the magnification hysteresis, thermal drift and lens distortion issues that hamper ex situ</i> DIC studies [56]. Similarly, imaging every step with two perpendicular raster directions served to minimize noise levels as only normal strain components are of interest here [57]. One drawback of the DIC method is the reduced number of strain measurement steps and the lengthy image acquisition times, compared with the continuous machine displacement output. One way to increase acquisition rate and resolution for future studies is to integrate a series of images with short dwell times at each hold [58]. However, this remains a point of debate within the DIC community in light of recent measurement of 5–12 us (noisy) beam settling times per pixel [59], which would encourage an early frame or pixel-time discard approach. Certainly, further selection and averaging for increased imaging quality could be considered, requiring an advanced, custom scan generator system [59]. Ultimately, the DIC is considered more direct and robust than the machine output, and the DIC-acquired elastic properties are accepted as true. With this considered, a variety of DIC observations need further discussion.

The DIC method provided high resolution evaluation of the local elastic strain during testing, revealing clear gradients for the Young's modulus across the PyC thickness. Improvements on resolution can provide unique insight to Poisson ratio dependencies as well. The first trend to discuss is the evolution of modulus with increasing pressure, this was observed via an inflection point in pillar 1, and also apparent in the machine output for both pillar 1 and 2. For example, the DIC modulus of row 6 transitioned from 66 GPa to 116 GPa. This phenomenon can be discussed in the context of PyC microstructure and defects. Recent studies have developed atomistic reconstruction of the PyC structure that suggest the turbostratic domains consist of curved planes, pentagon/heptagon interlayer connections, and nanoscale porosity [14,27,30]. It is proposed here that these defects may initially allow for compliant modes of elastic deformation. As the interlayer distance is compressed the system may stiffen as repulsive van der Waals interatomic potential takes over. From the perspective of composite interphase design, as it relates PyC deposition parameters and resulting crack deflection [60], the rate and magnitude of modulus increase would then depend on local defect density.

The next DIC observation provides unique and valuable insight into the PyC structure-property relationship. Both pillar 1 and 2 showed a spatial gradient of increasing modulus moving toward the fiber interface. This was complemented by the observed texture gradient from the OA analysis, that are likely intrinsically related to each other [14,28]. The gradients are respectively plotted as a function of estimated distance from the fiber surface in Fig. 14, where the shaded regions represent standard deviations of the data from pillar 1.

For pillar 1, E_z transitions from 66 to 150 GPa as the texture becomes more disordered toward the fiber surface. The change is dramatic relative to an OA shift of four degrees, but modelling efforts suggest this is not unrealistic. Farbos et al. predict that inter-domain misorientations of three degrees can impact the C_{11} stiffness tensor by 50 GPa [14]. Although evaluated for stiffness parallel to the basal plane, this acute orientation sensitivity suggests that the trends observed here are possible. Furthermore, the homogenization model presented by Böhlke found E_z ($\beta = 0$) range from 99 to 156 GPa when transitioning from HT to MT, shown in the table of Fig. 2. The HRTEM FFT OA was extracted from their figures, finding HT and MT equal to 50° and 60°, respectively. Although a factor of two larger, the ΔOA of ~10° spans the transition range
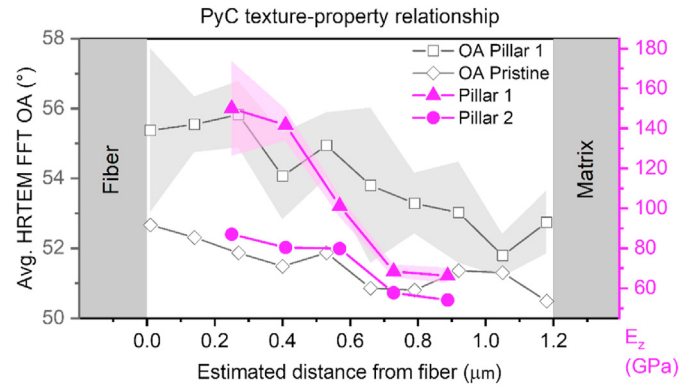

Fig. 14. Summary plot of experimental values for OA from HRTEM and E_z from DIC of the PyC for $\sigma_z < 2.5$ GPa. Values are arranged as a function of estimated distance from the fiber surface, providing a platform for composite interface design as it relates PyC properties to varying textures that can be tailored with different deposition parameters. (A colour version of this figure can be viewed online.)

observed in this experiment and shows similar change in modulus. Together, the results from Farbos and Böhlke et al. show acute misorientation sensitivity and provide confidence in the results. Continued modelling with high resolution of the misorientation dependence on the average c-axis stiffness is warranted to validate these findings. Pillar 2 shows E_z varying from 54 to 87 GPa across the same PyC thickness. The discrepancy between pillar 1 and pillar 2 may be a result of local texture variations during CVI deposition, or globular defect inclusions from the CVI process that were not captured in the thin TEM lamella taken from the center of the pillar [10,46]. It is shown that within pillar 1, the absolute texture and rate of change of texture across the PyC is larger compared with the pristine PyC. It is likely that local texture within pillar 2 is closer to that of the pristine PyC. Again, it is possible that the large compressive load achieved in pillar 1 resulted in basal plane slip and domain rotation, leading to more disordered texture and increased stiffness. The later cannot be proved since we cannot get spatially resolved textural information from the pillar prior to compression. Regardless the origin of the texture gradient, the trend supports that more uniform texture is directly related to a decreasing modulus. In order to understand the evolving property-structure relationships, it is important to consider fundamental PyC elasticity and why relatively large elastic moduli are observed in this case. As alluded to, most other experiments see average E_z ~25 GPa. Some show a similar texture dependence but are often less significant in both magnitude (ranging ± 10 GPa) and consistency, especially for the Z direction perpendicular to the graphitic planes [14,16,26]. DIC shows a factor of 2–5 times increased E_z depending on the local PyC texture and applied pressure. Two potential explanations were considered for the origin of the increased modulus. The first is extrinsic relating to boundary constraint and the other intrinsic as it relates to microstructural homogenization of elasticity.

The effect of constraint at the interfacing SiC boundaries is evaluated following a model system where the PyC is fully bound between two rigid substrates. Tsai presents an analytical solution relating the observed compression modulus, E_c, to the true modulus E in equations (1)–(3) where a, b, and t are the respective edge lengths and thickness of the bond layer [61].

$$\frac{E_c}{E} = \frac{1}{1-v^2}\left[1 + \frac{v^2}{1-2v}\left(1 - \frac{\tanh \alpha tS}{\alpha tS}\right)\right] \qquad (1)$$

$$\alpha = \frac{1}{t} \sqrt{\frac{6(1 - 2v)}{1 - v}} \qquad (2)$$

$$S = \frac{ab}{t(a + b)} \qquad (3)$$

Modelled values for Poisson ratio of high texture PyC are typically very low, $v_{zx} < 0.05$ [14]. Some experimental evaluations have found values as large as 0.35 [15], though likely this was amplified by bulk porosity effects. Here, the upper bound observed in this experiment, $v_{zx} = 0.25$, is taken as a conservative value for evaluation. The resulting observed modulus E_c would increase by 13%, which is significant but does not account the twofold increase observed with DIC. Additionally, it is likely only affecting the PyC boundaries, as observed in rows 1 and 7 that expressed outlier values as discussed above. The bulk (rows 2–6) of the modulus gradient appeared more intimately tied with the PyC texture and less with boundary constraint as the trend is linear with peak and minimum values observed toward the fiber and matrix interfaces, respectively. In the end, constraint is not expected to play a role in defining the true modulus across the entire bond layer.

The second and intrinsic explanation is related to findings from nanoscale elasticity models. MD simulations tend to agree with fundamental estimations for graphite and typical experimental values of $E_z \sim 25$ GPa [14,27]. These simulations have provided unique insight into the impact of local defect types; however, the length scale (8–12 nm edge length cubes) limits understanding of how long-range domain and domain boundary distributions may impact microscale elasticity. Böhlke et al. attempts to capture this on a slightly larger length scale with microstructures (LT, MT, and HT) defined by 50×50 nm^2 HRTEM images that captures tens to hundreds of domains. The homogenization technique, described by Fig. 2 in the introduction, finds mean values for E_z of ~99–156 GPa for HT and MT, respectively [29]. This is at the upper bound for DIC measurements observed in this study, with MT values ranging from 66 to 150 GPa. The slight overestimation by the homogenization model may be due to an assumption of perfectly bonded domains that omit boundary stiffness. It is conceivable that in a real system these boundaries provide an initial softening mode at low loads, similar to mechanisms discussed for modulus dependence on pressure, then transition to a stiffening mechanism by impeding basal plane slip and domain rotation. This would align with the modelled dependencies on L_c, where averaged domain stiffness in the c-axis increases with domain boundary cross-linking [14].

Ultimately, it is thought this study experimentally supports the homogenization theory where average domain misorientations generate a homogenized and globally increased modulus at this length scale. This explains the observed increase in modulus with increasing textural disorder. The homogenization method did not evaluate the texture dependence of Poisson's ratio. However, as texture becomes more turbulent, it can be inferred that the Poisson ratio would take on mixed character of the v_{zx} and v_{xz}. For v_{zx} and v_{xz}, Farbos et al. shows MD values of 0.05 and 1, respectively [14]. Gebert shows experimental values of 0.22 and 0.5, respectively [31]. However, most reported values simply assume a homogenous $v = 0.2$ [50,62]. With this wide range of values across length scales, the values and texture dependence observed with DIC is reasonable, however, improved DIC resolution is required for true quantification.

A final point of support for deformation mechanisms comes from a recent study by Zhang et al., that applied uniaxial micropillar compression to amorphous PyC [63]. The researchers presented values for modulus ~16–26 GPa that were fit to the loading curve. However, significant plastic deformation was observed in these pillars, attributed to interplanar bending and nanopore collapse, identified by accompanying MD simulations. For more accurate representation of the elasticity, the unloading modulus was evaluated (by this paper) and found to be ~50 GPa. This matches more closely to the values observed here. The PyC was fully amorphous, likely departing from the domain homogenization and boundary constraint effects, resulting in a slightly lower modulus than observed by the DIC. It can be noted here that the MD simulations in that study, and by Chen et al., support potential softening mechanisms by interplanar slip and defect distortion. However, it is still unclear if neighboring domains can provide a boundary locking mechanism that would homogenize and globally increase the observed modulus with increased pressure. These deformation mechanisms may support the theory that as medium texture domains bend and rotate, the local texture becomes more disordered, leading to increased stiffness observed in pillar 1 at high compressive stress.

To consolidate current observations of both models and experiments across length scales for medium to high texture PyC, a simple evaluation is proposed here. At the nanoscale (<50 nm), local PyC domain elasticity is dominated by the fundamental graphite structure with $E_z < 30$ GPa. At microscale (50 nm–5 μm), the long-range order with associated boundary and orientation distributions homogenize resulting in a relatively stiff matrix; modelled values range ~100–200 GPa and experiments range from 55 to 150 GPa, shown here to depend on both texture and pressure [17,28,63]. With increased deposition thickness, macroscale samples (>10 μm) are likely to contain large scale defects like porosity that may dominate, resulting in modulus values settling back around 5–30 GPa [10,16,17].

Lastly, in the context of composite design and modelling, an experimental method to identify properties and validate elasticity models at the microscale is of high value. During fabrication of SiC/SiC composites, it has been shown that thermo-elastic mismatch and fiber roughness can evolve compressive stresses normal to the PyC interface of 0.2–8 GPa [50]. The magnitude of residual stress can be tailored by varying the bond thickness and PyC modulus. A defined elasticity-texture relationship enables optimization of deposition parameters to minimize thickness and still promote deflection. The methodology presented here provides a path forward for defining and validating these necessary structure-property relationships.

5. Conclusion

This study combined micropillar compression and in situ DIC in a novel way to explore the elastic properties of the PyC interphase in as-fabricated SiC/PyC/SiC composites. HRTEM methods quantified PyC texture and domain size to complement the observed properties and define the structure-property relationships. Modulus values ranged from 55 to 150 GPa. The transition in stiffness is attributed to the evolution of domain misorientation since the domain size remained nearly constant across PyC thickness while modelling efforts support modulus sensitivity to OA. The elastic modulus also appeared to depend on applied pressure. It was postulated that compliant defects may stiffen as interatomic potential takes over. Quantification of the Poisson ratio was limited by SEM resolution, but qualitatively increased proportionally with OA. Ultimately, the large values of E_z and sensitivity to OA suggest that the elastic behavior of PyC follows the homogenization theory presented by Böhlke et al., but there is room for model development to capture 3D domain boundary effects. Micropillar DIC coupled with TEM offers a path forward to evaluate the true constitutive relationship between texture and microscale elasticity of PyC. This has significant implications on atomistic modelling to

interfacial design for composite optimization. Future campaigns would benefit from improved DIC resolution and a systematic study on highly controlled depositions to develop comprehensive and quantitative structure-property relationships. In situ TEM compression of PyC could also characterize domain and domain boundary deformation mechanisms in real time.

Declaration of competing interest

The authors declare that they have no known competing financial interests or personal relationships that could have appeared to influence the work reported in this paper.

Acknowledgements

References

[1] R.L. Seibert, B.C. Jolly, M. Balooch, D.P. Schappel, K.A. Terrani, Production and characterization of TRISO fuel particles with multilayered SiC, J. Nucl. Mater. 515 (Mar. 2019) 215–226, https://doi.org/10.1016/j.jnucmat.2018.12.024.

[2] F. Oveissi, S. Naficy, A. Lee, D.S. Winlaw, F. Dehghani, Materials and manufacturing perspectives in engineering heart valves: a review, in: Materials Today Bio, vol. 5, Elsevier B.V., Jan. 01, 2020, 100038, https://doi.org/10.1016/j.mtbio.2019.100038.

[3] Y. Katoh, et al., Continuous SiC fiber, CVI SiC matrix composites for nuclear applications: properties and irradiation effects, J. Nucl. Mater. 448 (1–3) (2014) 448–476, https://doi.org/10.1016/j.jnucmat.2013.06.040.

[4] S. Pompidou, J. Lamon, Analysis of crack deviation in ceramic matrix composites and multilayers based on the Cook and Gordon mechanism, Compos. Sci. Technol. 67 (10) (Aug. 2007) 2052–2060, https://doi.org/10.1016/j.compscitech.2006.11.013.

[5] M.Y. He, A.G. Anthony, J.W. Hutchinson, Crack deflection at an interface between dissimilar elastic materials: role of residual stresses, Int. J. Solid Struct. 31 (24) (1994) 3443–3455, https://doi.org/10.1016/0020-7683(94)90025-6.

[6] S. Daggumati, A. Sharma, A. Kasera, N. Upadhyay, Failure analysis of unidirectional ceramic matrix composite lamina and cross-ply laminate under fiber direction uniaxial tensile load: cohesive zone modeling and brittle fracture mechanics approach, J. Mater. Eng. Perform. 29 (4) (Apr. 2020) 2049–2060, https://doi.org/10.1007/s11665-020-04724-x.

[7] S. Bertrand, C. Droillard, R. Pailler, X. Bourrat, R. Naslain, TEM structure of (PyC/SiC) n multilayered interphases in SiC/SiC composites, J. Eur. Ceram. Soc. 20 (1–13) (2000), https://doi.org/10.1016/S0955-2219(99)00086-2.

[8] C. Fellah, J. Braun, C. Sauder, F. Sirotti, M.H. Berger, Influence of the carbon interface on the mechanical behavior of SiC/SiC composites, Compos. Part A Appl. Sci. Manuf. 133 (2020), 105867, https://doi.org/10.1016/j.compositesa.2020.105867. February.

[9] M. Seyring, A. Simon, I. Voigt, U. Ritter, M. Rettenmayr, Quantitative crystallographic analysis of individual carbon nanofibers using high resolution transmission electron microscopy and electron diffraction, Carbon N. Y. 116 (May 2017) 347–355, https://doi.org/10.1016/j.carbon.2017.01.107.

[10] E. López-Honorato, P.J. Meadows, P. Xiao, Fluidized bed chemical vapor deposition of pyrolytic carbon - I. Effect of deposition conditions on microstructure, Carbon N. Y. 47 (2) (Feb. 2009) 396–410, https://doi.org/10.1016/j.carbon.2008.10.023.

[11] A.A. Campbell, K.B. Campbell, G.S. Was, Anisotropy analysis of ultra-fine grain graphite and pyrolytic carbon, Carbon N. Y. 60 (2013) 410–420, https://doi.org/10.1016/j.carbon.2013.04.054.

[12] B. Reznik, D. Gerthsen, Microscopic study of failure mechanisms in infiltrated carbon fiber felts, Carbon N. Y. 41 (1) (Jan. 2003) 57–69, https://doi.org/10.1016/S0008-6223(02)00231-2.

[13] O.L. Blakslee, D.G. Proctor, E.J. Seldin, G.B. Spence, T. Weng, Elastic constants of compression-annealed pyrolytic graphite, J. Appl. Phys. 41 (8) (1970) 3373–3382, https://doi.org/10.1063/1.1659428.

[14] B. Farbos, J.P. Da Costa, G.L. Vignoles, J.M. Leyssale, Nanoscale elasticity of highly anisotropic pyrocarbons, Carbon N. Y. 94 (Aug. 2015) 285–294, https://doi.org/10.1016/j.carbon.2015.06.060.

[15] T.S. Gross, et al., Tension-compression anisotropy of in-plane elastic modulus for pyrolytic carbon, Carbon 49 (6) (May 01, 2011) 2145–2147, https://doi.org/10.1016/j.carbon.2011.01.012. Elsevier Ltd.

[16] T.S. Gross, N. Timoshchuk, I.I. Tsukrov, R. Piat, B. Reznik, On the ability of nanoindentation to measure anisotropic elastic constants of pyrolytic carbon, ZAMM - J. Appl. Math. Mech./Zeitschrift für Angew. Math. und Mech. 93 (5) (May 2013) 301–312, https://doi.org/10.1002/zamm.201100128.

[17] D. Liu, K. Mingard, O.T. Lord, P. Flewitt, On the damage and fracture of nuclear graphite at multiple length-scales, J. Nucl. Mater. 493 (Sep. 2017) 246–254, https://doi.org/10.1016/j.jnucmat.2017.06.021.

[18] H. Zhang, E. López-Honorato, P. Xiao, Fluidized bed chemical vapor deposition of pyrolytic carbon-III. Relationship between microstructure and mechanical properties, Carbon N. Y. 91 (May 2015) 346–357, https://doi.org/10.1016/j.carbon.2015.05.009.

[19] I.Y. Stein, et al., Structure-mechanical property relations of non-graphitizing pyrolytic carbon synthesized at low temperatures, Carbon N. Y. 117 (Jun. 2017) 411–420, https://doi.org/10.1016/j.carbon.2017.03.001.

[20] G. Savini, Y.J. Dappe, S. Öberg, J.C. Charlier, M.I. Katsnelson, A. Fasolino, Bending modes, elastic constants and mechanical stability of graphitic systems, Carbon N. Y. 49 (1) (Jan. 2011) 62–69, https://doi.org/10.1016/j.carbon.2010.08.042.

[21] J.P. Da Costa, P. Weisbecker, B. Farbos, J.M. Leyssale, G.L. Vignoles, C. Germain, Investigating carbon materials nanostructure using image orientation statistics, Carbon N. Y. 84 (C) (Apr. 2015) 160–173, https://doi.org/10.1016/j.carbon.2014.11.048.

[22] K. Jurkiewicz, et al., "Evolution of glassy carbon under heat treatment: correlation structure–mechanical properties, J. Mater. Sci. 53 (5) (Mar. 2018) 3509–3523, https://doi.org/10.1007/s10853-017-1753-7.

[23] P. Diss, J. Lamon, L. Carpentier, J.L. Loubet, P. Kapsa, Sharp indentation behavior of carbon/carbon composites and varieties of carbon, Carbon N. Y. 40 (14) (Jan. 2002) 2567–2579, https://doi.org/10.1016/S0008-6223(02)00169-0.

[24] C. Sauder, J. Lamon, R. Pailler, The tensile properties of carbon matrices at temperatures up to 2200 °c, Carbon N. Y. 43 (10) (Aug. 2005) 2054–2065, https://doi.org/10.1016/j.carbon.2005.03.020.

[25] S. Zhang, et al., Carbon nanotube reinforced strong carbon matrix composites, ACS Nano 14 (8) (2020) 9282–9319, https://doi.org/10.1021/acsnano.0c03268.

[26] H. Zhang, Mechanical and Microstructural Study of Silicon Carbide and Pyrolytic Carbon Coatings in Triso Fuel Particles, " The University of Manchester, 2012.

[27] M.W. Chen, B. Wu, L.C. Zhou, Y.B. Zhu, H.A. Wu, Micromechanical properties of pyrolytic carbon with interlayer crosslink, Carbon N. Y. 159 (Apr. 2020) 549–560, https://doi.org/10.1016/j.carbon.2019.12.096.

[28] T. Böhlke, T.-A. Langhoff, S. Lin, T. Gross, Homogenization of the elastic properties of pyrolytic carbon based on an image processing technique, ZAMM - J. Appl. Math. Mech./Zeitschrift für Angew. Math. und Mech. 93 (5) (May 2013) 313–328, https://doi.org/10.1002/zamm.201100180.

[29] S. Lin, T.A. Langhoff, T. Böhlke, Micromechanical estimate of the elastic properties of the coherent domains in pyrolytic carbon, Arch. Appl. Mech. 84 (1) (Jan. 2014) 133–148, https://doi.org/10.1007/s00419-013-0789-7.

[30] B. Farbos, et al., Nanoscale structure and texture of highly anisotropic pyrocarbons revisited with transmission electron microscopy, image processing, neutron diffraction and atomistic modeling, Carbon N. Y. 80 (1) (Dec. 2014) 472–489, https://doi.org/10.1016/j.carbon.2014.08.087.

[31] J.M. Gebert, et al., Elastic constants of high-texture pyrolytic carbon measured by ultrasound phase spectroscopy, Carbon 48 (12) (Oct. 01, 2010) 3647–3650, https://doi.org/10.1016/j.carbon.2010.06.002. Elsevier Ltd.

[32] T.J. Marrow, et al., In situ measurement of the strains within a mechanically loaded polygranular graphite, Carbon N. Y. 96 (Jan. 2016) 285–302, https://doi.org/10.1016/j.carbon.2015.09.058.

[33] J. Kabel, et al., Micro-Mechanical evaluation of SiC-SiC composite interphase properties and debond mechanisms, Compos. B Eng. 131 (2017) 1–18, https://doi.org/10.1016/j.compositesb.2017.07.035.

[34] T.E.J. Edwards, et al., Deformation of lamellar γ-TiAl below the general yield stress, Acta Mater. 163 (Jan. 2019) 122–139, https://doi.org/10.1016/j.actamat.2018.09.061.

[35] F. Di Gioacchino, W.J. Clegg, Mapping deformation in small-scale testing, Acta Mater. 78 (Oct. 2014) 103–113, https://doi.org/10.1016/j.actamat.2014.06.033.

[36] T.E.J. Edwards, F. Di Gioacchino, G. Mohanty, J. Wehrs, J. Michler, W.J. Clegg, Longitudinal twinning in a TiAl alloy at high temperature by in situ microcompression, Acta Mater. 148 (Apr. 2018) 202–215, https://doi.org/10.1016/j.actamat.2018.01.007.

[37] T.E.J. Edwards, F. Di Gioacchino, H.P. Springbett, R.A. Oliver, W.J. Clegg, Stable speckle patterns for nano-scale strain mapping up to 700 °C, Exp. Mech. 57 (9) (Nov. 2017) 1469–1482, https://doi.org/10.1007/s11340-017-0317-8.

[38] T.E.J. Edwards, et al., Transverse deformation of a lamellar TiAl alloy at high temperature by in situ microcompression, Acta Mater. 166 (Mar. 2019) 85–99, https://doi.org/10.1016/j.actamat.2018.11.050.

[39] T.E.J. Edwards, F. Di Gioacchino, A.J. Goodfellow, W.J. Clegg, Slip bands in lamellar TiAl during high cycle fatigue microcompression by correlative total strain mapping, diffraction orientation mapping and transmission electron

imaging, Int. J. Fatig. 124 (Jul. 2019) 520—527, https://doi.org/10.1016/j.ijfatigue.2019.03.016.

[40] R.D. Jones, et al., Reduced partitioning of plastic strain for strong and yet ductile precipitate-strengthened alloys, Sci. Rep. 8 (1) (Dec. 2018) 1—14, https://doi.org/10.1038/s41598-018-26917-0.

[41] J.T. Pürstl, et al., On the extraction of yield stresses from micro-compression experiments, Mater. Sci. Eng., A (Sep. 2020), 140323, https://doi.org/10.1016/j.msea.2020.140323.

[42] L. Chen, T.E. James Edwards, F. Di Gioacchino, W.J. Clegg, F.P.E. Dunne, M.S. Pham, Crystal plasticity analysis of deformation anisotropy of lamellar TiAl alloy: 3D microstructure-based modelling and in-situ microcompression, Int. J. Plast. 119 (Aug. 2019) 344—360, https://doi.org/10.1016/j.ijplas.2019.04.012.

[43] D. Schawaller, B. Clauß, M.R. Buchmeiser, "Ceramic Filament Fibers - A Review," Macromolecular Materials and Engineering, vol. 297, John Wiley & Sons, Ltd, Jun. 01, 2012, pp. 502—522, https://doi.org/10.1002/mame.201100364, 6.

[44] J. Lamon, S. Mazerat, M. R'Mili, Reinforcement of ceramic matrix composites: properties of SiC-based filaments and tows, in: Ceramic Matrix Composites, John Wiley & Sons, Inc., Hoboken, NJ, USA, 2014, pp. 1—26.

[45] L.L. Snead, T. Nozawa, Y. Katoh, T.S. Byun, S. Kondo, D.A. Petti, Handbook of SiC properties for fuel performance modeling, J. Nucl. Mater. 371 (1—3) (2007) 329—377, https://doi.org/10.1016/j.jnucmat.2007.05.016.

[46] J. Kabel, et al., A novel fiber-fretting test for tribological characterization of the fiber/matrix interface, Compos. B Eng. 206 (Feb. 2021), 108535, https://doi.org/10.1016/j.compositesb.2020.108535.

[47] H. Zhang, B.E. Schuster, Q. Wei, K.T. Ramesh, The design of accurate micro-compression experiments, Scripta Mater. 54 (2) (2006) 181—186, https://doi.org/10.1016/j.scriptamat.2005.06.043.

[48] I.N. Sneddon, The relation between load and penetration in the axisymmetric boussinesq problem for a punch of arbitrary profile, Int. J. Eng. Sci. 3 (1) (May 1965) 47—57, https://doi.org/10.1016/0020-7225(65)90019-4.

[49] Y.-S. Jeong, K. Choi, H.G. Yoon, Microstructural control of pyrolytic carbon layer deposited from methane by isotropic chemical vapor infiltration, J. Korean Ceram. Soc. 56 (3) (2019) 291—297, https://doi.org/10.4191/kcers.2019.56.3.09.

[50] E. Buet, C. Sauder, D. Sornin, S. Poissonnet, J. Rouzaud, C. Vix-guterl, Influence of surface fibre properties and textural organization of a pyrocarbon interphase on the interfacial shear stress of SiC/SiC minicomposites reinforced with Hi-Nicalon S and Tyranno SA3 fibres, J. Eur. Ceram. Soc. 34 (2) (2014) 179—188, https://doi.org/10.1016/j.jeurceramsoc.2013.08.027.

[51] J. Schindelin, et al., Fiji: an open-source platform for biological-image analysis, Nat. Methods 9 (7) (Jul. 28, 2012) 676—682, https://doi.org/10.1038/nmeth.2019. Nature Publishing Group.

[52] F. Tuinstra, J.L. Koenig, "Raman Spectrum Of Graphite, J. Chem. Phys. 53 (3) (Aug. 1970) 1126—1130, https://doi.org/10.1063/1.1674108.

[53] Y.S. Choi, M.D. Uchic, T.A. Parthasarathy, D.M. Dimiduk, Numerical study on microcompression tests of anisotropic single crystals, Scripta Mater. 57 (9) (Nov. 2007) 849—852, https://doi.org/10.1016/j.scriptamat.2007.06.057.

[54] S. Pathak, et al., Strong, ductile, and thermally stable bcc-Mg nanolaminates, Sci. Rep. 7 (1) (Dec. 2017) 1—9, https://doi.org/10.1038/s41598-017-08302-5.

[55] W.C. Oliver, G.M. Pharr, Measurement of hardness and elastic modulus by instrumented indentation: advances in understanding and refinements to methodology, J. Mater. Res. 19 (1) (2004) 3—20, https://doi.org/10.1557/jmr.2004.19.1.3.

[56] A.W. Mello, T.A. Book, A. Nicolas, S.E. Otto, C.J. Gilpin, M.D. Sangid, Distortion correction protocol for digital image correlation after scanning electron microscopy: emphasis on long duration and ex-situ experiments, Exp. Mech. 57 (9) (Nov. 2017) 1395—1409, https://doi.org/10.1007/s11340-017-0303-1.

[57] A.M. Korsunsky, M. Sebastiani, E. Bemporad, Residual stress evaluation at the micrometer scale: analysis of thin coatings by FIB milling and digital image correlation, Surf. Coating. Technol. 205 (7) (Dec. 2010) 2393—2403, https://doi.org/10.1016/j.surfcoat.2010.09.033.

[58] C. Mansilla, V. Ocelík, J.T.M. De Hosson, A new methodology to analyze instabilities in SEM imaging, Microsc. Microanal. 20 (6) (Sep. 2014) 1625—1637, https://doi.org/10.1017/S1431927614013282.

[59] W.C. Lenthe, J.C. Stinville, M.P. Echlin, Z. Chen, S. Daly, T.M. Pollock, Advanced detector signal acquisition and electron beam scanning for high resolution SEM imaging, Ultramicroscopy 195 (Dec. 2018) 93—100, https://doi.org/10.1016/j.ultramic.2018.08.025.

[60] J. Kabel, et al., Ceramic composites: a review of toughening mechanisms and demonstration of micropillar compression for interface property extraction, J. Mater. Res. 33 (4) (Feb. 2018) 424—439, https://doi.org/10.1557/jmr.2017.473.

[61] H.C. Tsai, Compression analysis of rectangular elastic layers bonded between rigid plates, Int. J. Solid Struct. 42 (11—12) (Jun. 2005) 3395—3410, https://doi.org/10.1016/j.ijsolstr.2004.10.015.

[62] T. Nozawa, Y. Katoh, L.L. Snead, The effect of neutron irradiation on the fiber/matrix interphase of silicon carbide composites, J. Nucl. Mater. 384 (3) (2009) 195—211, https://doi.org/10.1016/j.jnucmat.2008.11.015.

[63] X. Zhang, et al., Theoretical strength and rubber-like behaviour in micro-sized pyrolytic carbon, Nat. Nanotechnol. 14 (8) (Aug. 2019) 762—769, https://doi.org/10.1038/s41565-019-0486-y.